Correlation between Nonlinear Optical Properties and Electronic Band Modification in Cobalt-Doped ZnO Nanorods

Mrinal K. Sikdar, Nitul S. Rajput, Ajanta Maity, and Pratap K. Sahoo*
School of Physical Sciences, National Institute of Science Education and Research, HBNI, Jatni 752050, India

(Received 20 December 2019; revised 4 May 2020; accepted 3 June 2020; published 16 July 2020)

We report a study on the nonlinear optical properties of cobalt- (Co) doped ZnO nanorods (NRs) using the single-beam *Z*-scan technique. In the open-aperture measurements, the undoped sample shows two-photon absorption (TPA) characteristics, whereas the doped samples exhibit a saturable absorption (SA) signature. In the closed-aperture measurements, all the samples show a self-defocusing behavior. We correlate the nonlinear absorption coefficient with the exponential reduction of the optical band gap and explain it in terms of electronic-band-structure modification because of doping. Density-functional-theory calculation is also used to understand the observed nonlinear absorption and band-gap variation. The present study can help to understand the origin of SA in ZnO. Doped ZnO nanorods can illustrate high SA and nonlinear refraction by appropriate Co doping, which can drive the technology for *Q* switching and mode locking in solid-state and fiber lasers.

DOI: 10.1103/PhysRevApplied.14.014050

I. INTRODUCTION

As it is a transparent conducting oxide (TCO), ZnO is a promising candidate for designing nonlinear optical [1] and optoelectronic [2] devices due to its high nonlinear optical coefficient and unique optical properties, such as the wide direct band gap of 3.2 eV and a large exciton binding energy of 60 meV. ZnO inherently possess high optical nonlinearity because of the unequal atomic dimensions of the Zn and O atoms and the high polar potentials of the ZnO crystal [3–5]. Hence, both intrinsic [6] and impurity-related [3,7] defects affect its nonlinear optical characteristics. ZnO is also robust, with minimum optical damage [8], inexpensive, widely available, nontoxic, and has a fast recovery time (1–5 ps) [9], which makes it a suitable candidate for designing solid-state and fiber lasers. Fiber lasers are one of the latest developments in laser technology, with a wide range of applications [10]. They are compact, efficient, and can produce highly coherent and ultralow-noise laser beams [10,11]. In the field of photonics, materials exhibiting two-photon absorption (TPA) are used in autocorrelators and optical power limiters [12], whereas the phenomenon of saturable absorption (SA) is used in passive mode locking, *Q* switching of lasers, and laser resonators [13].

The optical properties of ZnO also depend on the shape and size of the nanostructures. It has been reported that ZnO can be grown in a variety of subwavelength-sized nanostructures [14] for a wide range of applications [15] in sensors [16], light-emitting diodes and lasing [17], and dye-sensitized solar cells [18,19]. The physical and chemical properties of these nanostructures can be varied greatly with the method of preparation adopted [6,14,20]. The optical and electrical properties can be tuned further by doping with various impurities [2,21,22]. In particular, the doping of ZnO with transition metals such as cobalt adds local magnetic moments and alters the electronic structure in the crystal matrix locally, thus giving rise to magnetic and spin-dependent phenomena [23] and also tuning the optical band gap [24,25]. These materials are known as dilute magnetic semiconductors (DMS) and they can be used in next-generation magneto- or spin-based optoelectronics [26].

The ferromagnetic ordering can give rise to magnetization-induced modifications in the nonlinear optical properties of the material [3]. However, the effect of the electronic band modification on the nonlinear optical properties and the origin of the saturable absorption phenomenon in ZnO has not been explored comprehensively.

In this study, we investigate the defect-induced electronic band-gap tunability by cobalt doping in hydrothermally grown ZnO nanorods (NRs) and we correlate with how that affects the nonlinear optical properties using a single-beam *Z*-scan technique.

II. THEORETICAL METHODS AND EXPERIMENTAL DETAILS

The theoretical calculations on the pristine and Co-doped ZnO are done using the Vienna Ab initio Simulation Package (VASP) code [27–29] based on density-functional

*pratap.sahoo@niser.ac.in

theory (DFT). The plane-wave basis set is implemented in the VASP code. For our calculations, we use the generalized gradient approximation (GGA) along with the Perdew-Burke-Ernzerhof (PBE) functional and the default projector-augmented-wave (PAW) potentials.

The optimized atomic configurations for the theoretical calculations are shown in Fig. 1. ZnO has a wurtzite structure belonging to the hexagonal crystal system and the space group is $P6_3mc$. The ZnO crystal consists of alternating Zn and O planes stacked along the c axis and the Zn^{2+} and O^{2-} ions are tetrahedrally coordinated. After optimization of the atomic configurations, we perform the self-consistent calculation using the plane-wave basis set with a 500-eV energy cutoff and the Brillouin zone is sampled using $12 \times 12 \times 6$ gamma-point grids. Full atomic relaxations are made using convergence parameters up to 0.001 eV/Å for the atomic forces and less than 1 meV for the total energy. The optimized lattice parameters for pristine ZnO are $a = 3.288$ Å and $c = 5.311$ Å. Using the standard pseudopotentials, Zn $3d^{10}4s^2$, Co $3d^8 4s^1$, and O $2s^2 2p^4$ are treated as valence electrons. A 64-atom supercell of Co-doped ZnO is taken, where one of the Zn atoms is replaced with a Co atom, which results in 3.125% Co doping in ZnO, and the lattice parameters of the optimized supercell are found to be same as that of the pristine ZnO.

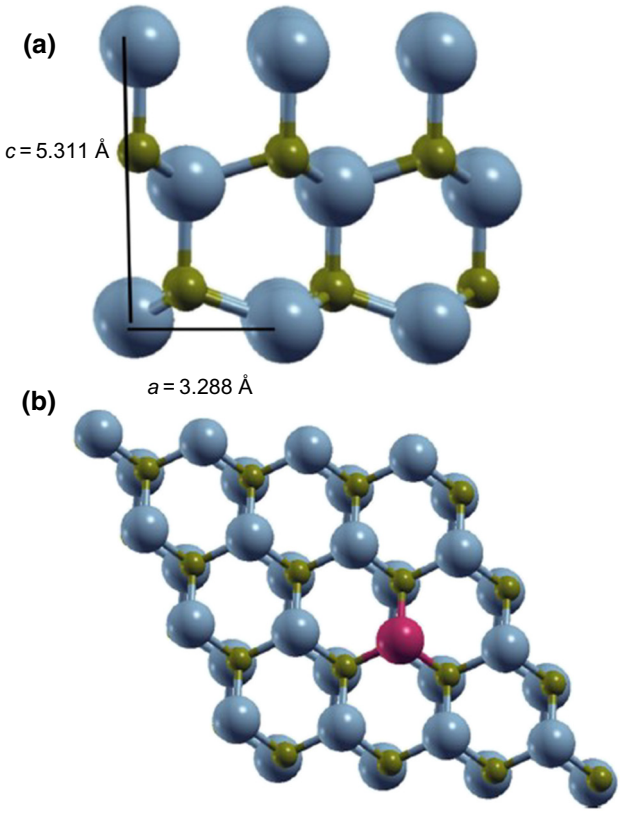

FIG. 1. The optimized atomic configurations of (a) pristine and (b) cobalt-doped ZnO used for the theoretical calculations. The Zn, O, and Co atoms are shown in blue, green, and pink, respectively.

A hydrothermal process [30,31] is used to grow the nanorods. For the growth of the ZnO nanorods, zinc nitrate $[Zn(NO_3)_2.6H_2O]$ and hexamethylenetetramine (HMT) $[(CH_2)_6N_4]$ are used as precursor chemicals. $Co(NO_3)_2.6H_2O$ is used as the source of Co in the doped samples. A solution containing an equimolar concentration of 0.05 M zinc nitrate and 0.05 M HMT is prepared in deionized water and stirred at room temperature for 15–30 min. To provide seeding for the ZnO nanorods, silicon and quartz substrates are coated with 0.01 M zinc-oxide nanopowder (< 100 nm, Sigma-Aldrich) solution in deionized water, using a spin-coating unit. These nanoparticles provide nucleation sites for the ZnO NRs, for better uniformity of growth throughout the surface of the substrate. The coated substrates are then glued to a glass slide and dipped into the precursor solution. The vessel is sealed and placed inside a hot-water bath for 3 h. The temperature of the water bath is kept at 80 °C. Once the growth is completed, the substrates are cleaned using deionized water to remove any residue left and then dried.

The morphology of the grown samples is examined using a field-emission scanning electron microscope (FESEM). Subsequently, spectroscopic studies such as Raman spectroscopy and photoluminescence study are carried out using a Raman-photoluminescence system (Jobin-Yvon LabRam HR Evolution, Horiba). A 532-nm laser is used for Raman excitation and a 325-nm He-Cd laser is used for the photoluminescence (PL) measurements. Optical measurements (absorbance) of the samples are carried out using a UV-VIS-NIR spectrometer (Shimadzu). The x-ray diffraction spectra for the study of crystal structure and phases of the NRs are studied using a Rigaku Smartlab x-ray diffractometer with Cu Kα ($\lambda = 1.5418$ Å). Structural and chemical analyses of selected samples are performed using a transmission-electron-microscopy (TEM) system. The TEM system (JEM-F200, JEOL) is equipped with a $4k \times 4k$ imaging detector with real-time drift-correction technology (Gatan Inc.). The integrated energy-dispersive x-ray spectrometer (JED-2300 Series) is used for elemental mapping of the NRs.

The third-order nonlinear optical (NLO) properties of the ZnO NRs are studied using a single-beam Z-scan technique [32]: the experimental setup is shown in Fig. 2. The nonlinear absorption coefficient (β) and the nonlinear refraction (n_2) are measured by the open-aperture (OA) and closed-aperture (CA) Z scan, respectively. In OA measurements, the aperture is removed, which allows the photodetector to capture the total transmitted power from the sample, and any variation in transmittance is due to nonlinear absorption by the sample. In CA measurements, an aperture is placed in front of the photodetector and a fraction of the transmitted beam from the sample is monitored.

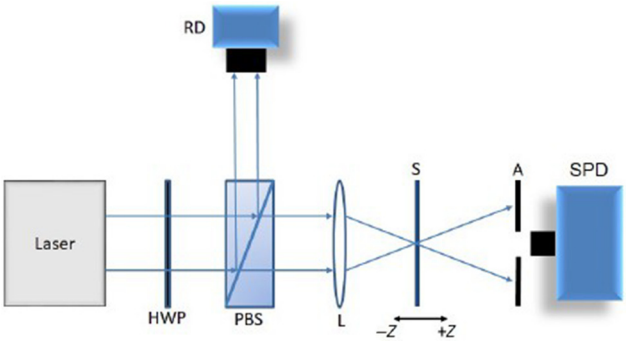

FIG. 2. The single-beam Z-scan experimental setup: HWP, half-wave plate; PBS, polarizing beam splitter; L, lens (200 mm); S, sample; A, aperture; RD, reference detector; SPD, signal photodetector.

The sample acts as a weak nonlinear lens and small distortions in this beam depend on the nonlinear refraction. In our experiment, the samples are irradiated using a nanosecond Q-switched diode-pumped solid-state laser centered at wavelength $\lambda = 532$ nm. The laser delivers a linearly polarized pulse in a Gaussian-transverse-electromagnetic-(TEM_{00}) mode intensity profile. For our measurements, the laser is operated at a repetition rate of 40 kHz with a pulse duration of 1.1 ns. A converging lens (focal length $f = 20$ cm) is used to focus the laser beam on the sample, with a spot size of $w_0 \approx 52$ μm. Therefore, the Rayleigh length ($z_0 = \pi w_0^2/\lambda$) is approximately 16 mm, which is much larger than the "sample plus substrate" thickness. The peak intensity at the focal point is 6.66×10^7 W/cm^2. A motorized translation stage is used to move the sample through a distance of 10 cm along the z axis and the focal plane.

III. RESULTS AND DISCUSSION

Figure 3 shows the SEM and TEM images of the grown ZnO nanorods (undoped). We observe two distinct types of size distribution in the grown samples. The smaller NRs typically have a diameter of 200 nm and a length of 500 nm (type I). The larger NRs are of 0.5–1.5 μm in diameter and have a length of 5–10 μm (type II). Multiple nanorods also cluster together to form a starlike morphology. Both types of NRs have a hexagonal form with a nearly smooth surface. We also observe similar morphological characteristics in the doped ZnO NRs. From the high-resolution TEM (HRTEM) image, we find the spacing between the lattice planes to be 0.26 nm. The NRs grow along the [0001] direction, i.e., the c axis. The TEM–energy-dispersive x-ray spectroscopy (TEM-EDS) mapping of a Co-doped ZnO NR is shown in Fig. S1 (see the Supplemental Material [33]).

The x-ray diffraction (XRD) patterns of the undoped and doped ZnO NRs are shown in Fig. 4. From the XRD patterns, we see that the samples thus prepared are of a

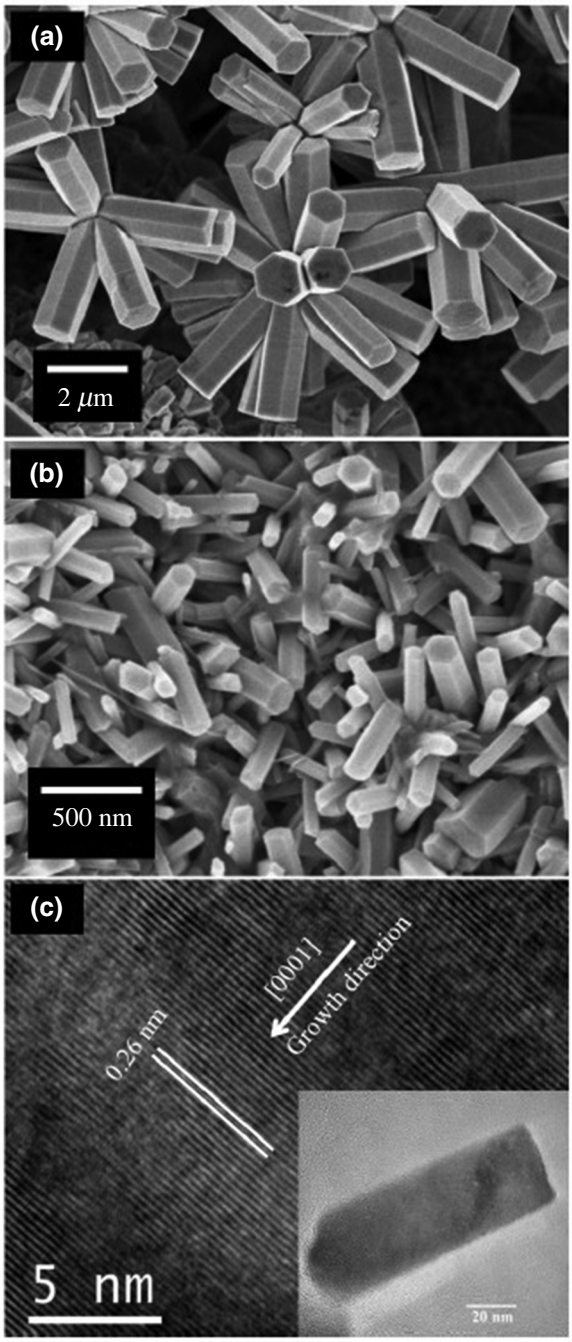

FIG. 3. SEM images of the grown ZnO nanorods (undoped). (a) Both smaller (type I) and larger (type II) NRs can be seen. (b) Grown NRs of type I. (c) A HRTEM image of a 5% Co-doped ZnO NR. The inset shows a TEM image of the same nanorod.

hexagonal wurtzite crystal structure and are in good agreement with the standard JCPDS database of card number 36-1451. The absence of secondary phases suggests that the Zn^{2+} sites in the crystal are successfully substituted by Co^{2+} ions. A peak at approximately 51.4° corresponds to that of the Si substrate (JCPDS 72-1088). In the tetrahedral coordination, the ionic radius of Co^{2+} (0.58 Å) is

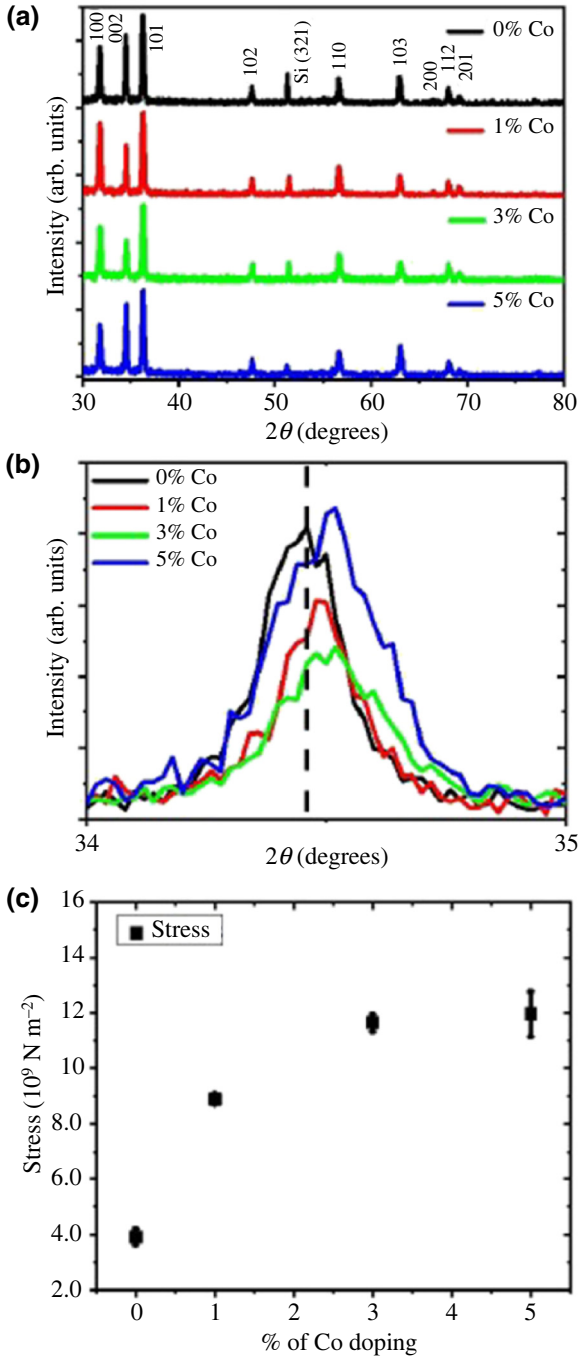

FIG. 4. (a) The XRD pattern of the as-prepared undoped and doped ZnO NRs. (b) A magnified view of the (002) phase of the NRs. (c) A plot of the stress versus the percentage of Co doping.

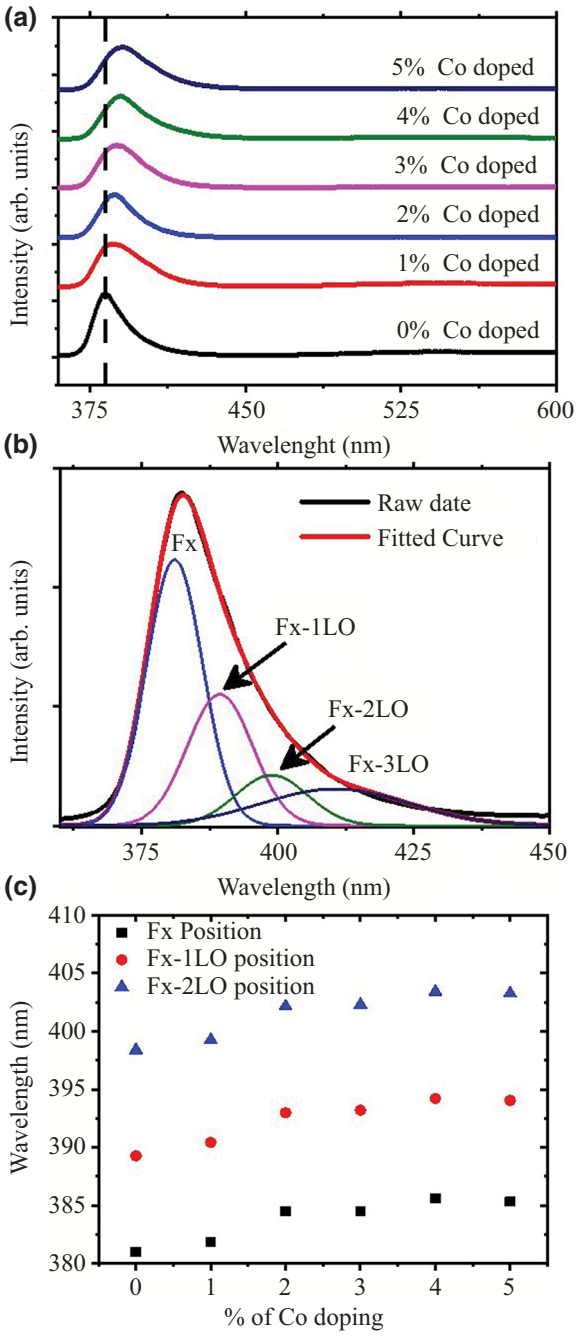

FIG. 5. (a) Room-temperature PL spectra of the grown undoped ZnO and doped ZnO NRs. (b) The deconvoluted peaks of the undoped sample. (c) The variation of the Fx, Fx-1LO, and Fx-2LO peaks with the percentage of Co doping in ZnO NRs.

smaller than that of Zn^{2+} (0.60 Å), so the lattice parameters should decrease, giving rise to compressive strain. We see in Fig. 4(b) that the (002) diffraction peak shifts toward higher 2θ values with increasing Co doping, which suggests that there is a contraction of the unit cell, i.e., the lattice parameters are decreasing [34,35], and the peaks are also broadened, which suggests the formation of smaller crystallites. The lattice parameters and the strain and stress values are calculated using the formulas in Refs. [36–38] and are summarized in Table S1 (see the Supplemental Material [33]). The positive stress value indicates that the crystal lattice is in a compressed state and we see from Fig. 4(c) that the stress increases with the increase of Co doping.

Room-temperature photoluminescence (PL) spectra collected from the undoped and doped nanorods are shown in Fig. 5. For all the samples, a very strong peak appears at 382 nm. This UV peak corresponds to the near-band-edge (NBE) exciton decay of ZnO and it is red shifted for the Co-doped samples [39]. The observed red shift and broadening occur due to the change of the band gap due to doping [40], which is further evident from subsequent UV-vis absorbance spectra and DFT calculations. The NBE peaks for the undoped ZnO nanorods are deconvoluted and are shown in Fig. 5(b). Four subpeaks are found under the NBE envelope. The first one, which is known as the Fx (free excitons) peak, appears at approximately 381 nm. Subsequent longitudinal-optical (LO) exciton-phonon interaction peaks appear at approximately 389 nm (Fx-1LO) and approximately 399 nm (Fx-2LO) and the last weak peak appears at approximately 407 nm (Fx-3LO). It is noted that the peak positions are red shifted and broadened with the amount of doping, which can happen when the electrons get trapped in the impurity-related defect states below the conduction band. Along with the Fx peak, the wavelength of the other LO peaks also increases with the Co doping, and they are shown in Fig. 5(c). However, the energy separation between the Fx and Fx-1LO peaks for the different samples remains nearly constant (approximately 71 meV), which signifies that the energy of the 1LO phonon remains almost unchanged. Thus, the Frohlich interaction remains nearly the same at room temperature for all the samples.

The linear optical absorbance of the samples over a wide range of light wavelengths from 300 to 800 nm is shown in Fig. 6(a). The samples are transparent in the visible region and remain active in the UV region. It is also observed that the absorption edge of the samples is red shifted with the doping concentration. Further, the optical band gaps of the samples are calculated using the Tauc plot. The band gap for pristine ZnO nanorods is found to be 3.07 eV. For the 1% Co-doped NRs, the band gap is 2.88 eV, which is a 6.1% drop from the pristine value. The band gap keeps on decreasing with the amount of doping [41]. However, from 1% onward, the change in the band gaps with the percentage of Co doping drops slowly (0.5%) as compared to the

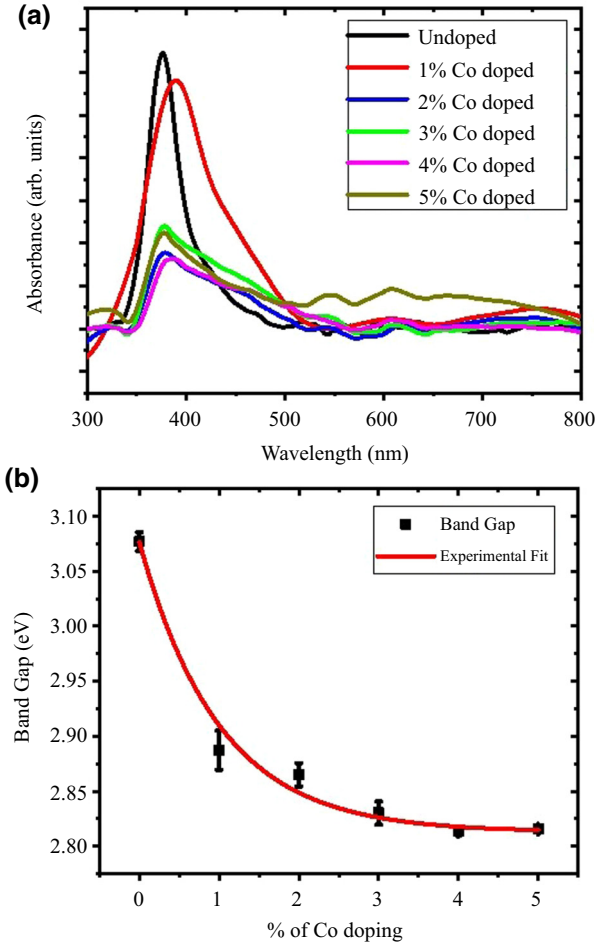

FIG. 6. (a) The UV-vis absorbance spectra obtained from the grown NRs. (b) The obtained optical band gaps of the NRs, calculated using the Tauc method.

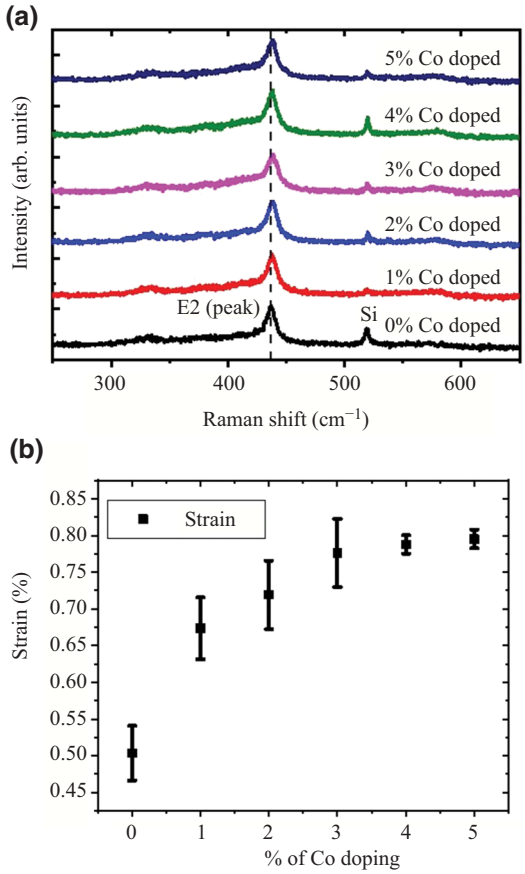

FIG. 7. (a) Raman spectra obtained from the samples. (b) A plot of the strain calculated versus the percentage of Co doping in ZnO.

6.1% drop in the case of pristine ZnO. The drop in the band gaps follows an approximately exponential pattern, which is shown in Fig. 6(b).

Raman spectra obtained from the samples are shown in Fig. 7(a). The presence of an E2 (high) peak at around 438 cm^{-1} with high intensity is observed. The E2 (high) phonon frequency is dependent on the residual stress in the wurtzite crystal of ZnO. It is found that the position of the E2 (high) peak gradually shifts toward higher frequency with the doping concentration [35]. The shift of the E2 (high) peak is due to the formation of compressive stress in the crystal lattice due to Co doping. This observation is in good agreement with our XRD results. To calculate the strain in the crystal lattice, we fit the experimental E2 (high) peak with a Lorentzian function [42] and use the given relation in the reference [43]. The position of the E2 (high) mode for bulk ZnO is taken to be 434 cm^{-1} [44]. Table S2 (see the Supplemental Material [33]) and Fig. 7(b) summarize the strain calculated from the Raman spectra with various Co-doping concentrations. The strain calculated from the Raman spectra is higher than that from the XRD data [45].

Open-aperture (OA) and closed-aperture (CA) Z-scan curves for the ZnO NRs as a function of the cobalt doping are shown in Figs. 8 and 9. In the OA Z-scan curves, we see that for the undoped sample, the transmittance curve shows a valley at the focal plane, which is a signature of the TPA phenomenon, whereas for all the doped samples, a transmittance peak is observed at the focal plane, which is a signature of SA. A prefocal maxima is followed by a postfocal minima in the CA Z-scan curves for all the samples. This is the signature of the self-defocusing effect, which corresponds to a negative value of the nonlinear refractive index. In the OA [Eq. (1)] and CA [Eq. (2)] configurations, the normalized transmittance for the Z-scan measurements is given as [3,32],

$$T(z, S = 1) = 1 - \frac{\beta I_0 L_{\text{eff}}}{2^{1.5}(1 + x^2)}, \tag{1}$$

$$T(z, \Delta\phi_0) = 1 - \frac{4\Delta\phi_0 x}{(x^2 + 9)(x^2 + 1)} - \frac{2(x^2 + 3)\Delta\Psi_0}{(x^2 + 9)(x^2 + 1)}, \tag{2}$$

where β is the nonlinear absorption coefficient, I_0 is the peak intensity at the focal point ($z = 0$), $x = z/z_0$, and L_{eff} is the effective length of the sample, given as $L_{\text{eff}} = (1 - e^{-\alpha L})/\alpha$, where α is the absorption coefficient and L is the sample thickness. $S = 1$ corresponds to OA configuration measurements. $\Delta\phi_0 = kn_2 I_0 L_{\text{eff}}$ and $\Delta\psi_0 = \beta I_0 L_{\text{eff}}/2$ are the phase-change terms due to nonlinear refraction and nonlinear absorption, respectively. Here, $k = 2\pi/\lambda$, n_2 is the nonlinear refractive index. β is positive for TPA and negative for SA.

Table I shows the comparison of the β and n_2 values of ZnO thin films and NRs using 532-nm excitation from previous reports and the present study. To obtain the β and

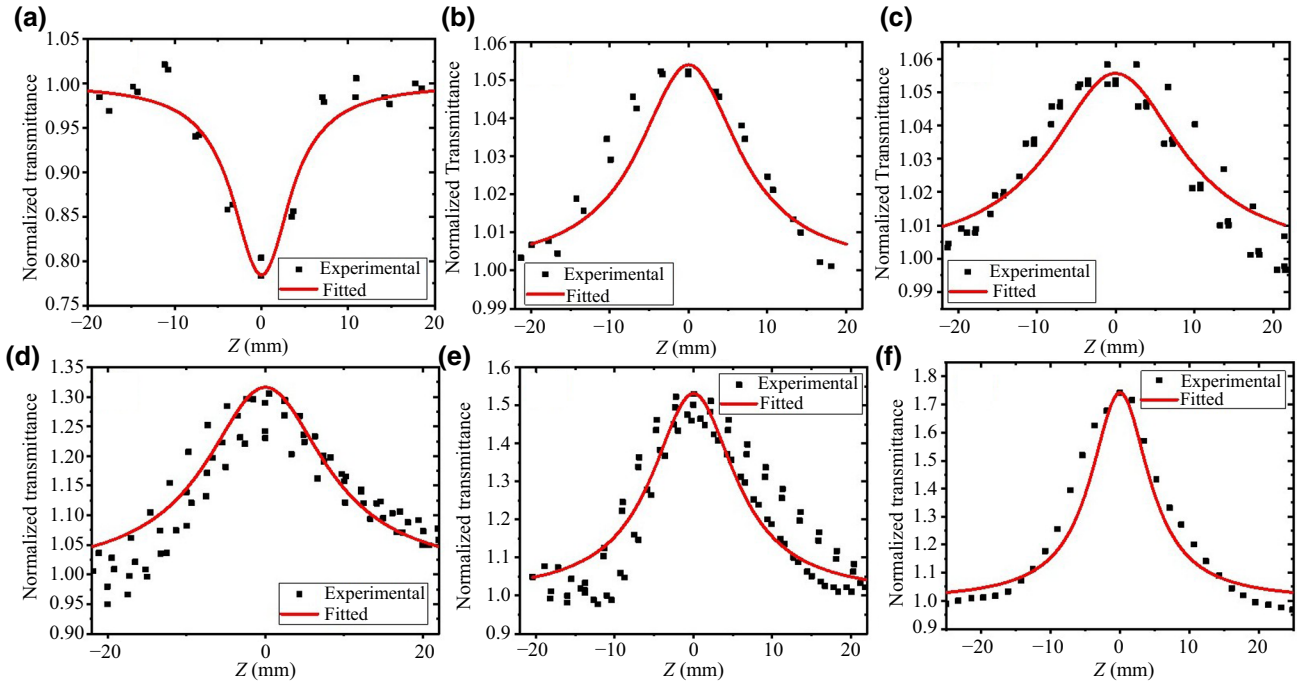

FIG. 8. Open-aperture (OA) Z-scan curves for the ZnO NRs with different amounts of cobalt doping: (a) undoped; (b) 1% Co doped; (c) 2% Co doped; (d) 3% Co doped; (e) 4% Co doped; (f) 5% Co doped.

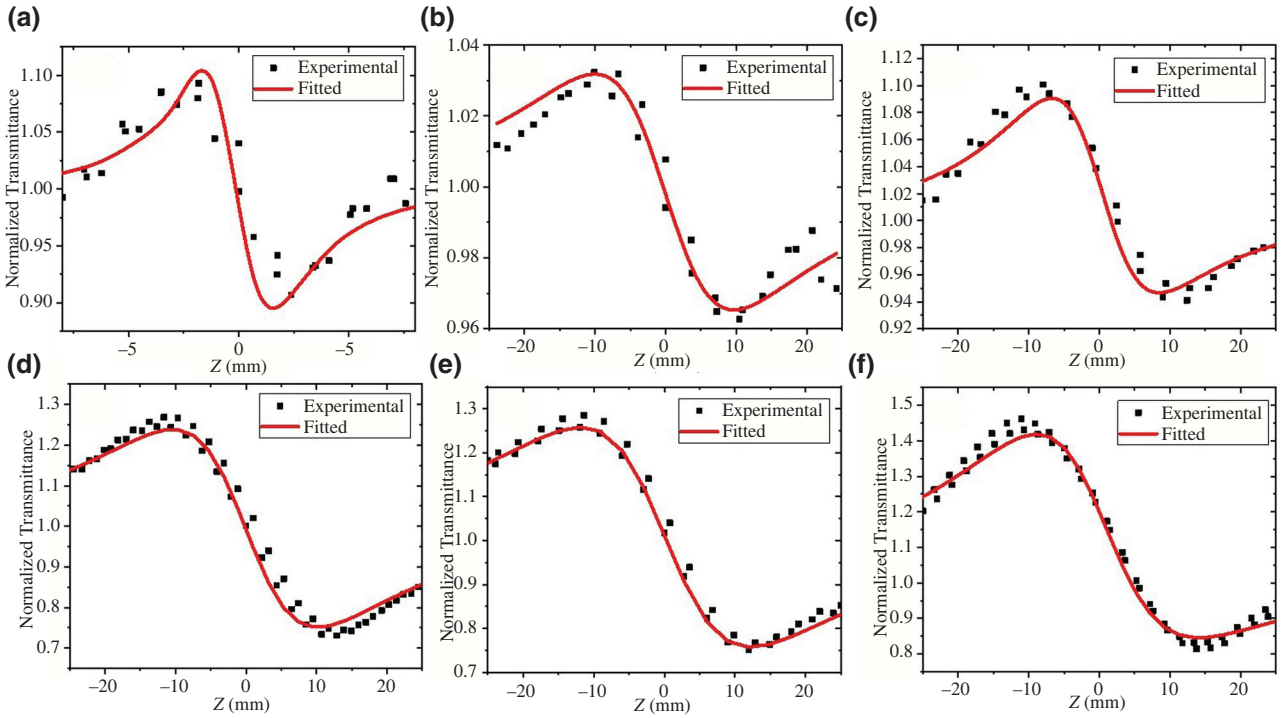

FIG. 9. Closed-aperture (CA) *Z*-scan curves for the ZnO NRs with different amounts of cobalt doping: (a) undoped; (b) 1% Co doped; (c) 2% Co doped; (d) 3% Co doped; (e) 4% Co doped; (f) 5% Co doped.

n_2 values, we fit the experimental *Z*-scan traces with Eqs. (1) and (2). The obtained β and n_2 values are higher compared to those previously reported for ZnO thin films and NRs, which is due to the cobalt doping and the geometrical arrangements of the NRs. There is a local enhancement of the field due to Fabry–Perot-like localized resonance, which arises from the small-scale ordering of the NRs [3]. This local enhancement of the field, defect states, and the heating effect due to the high-power laser excitation and the high repetition rate all contribute to the increase in the nonlinear interactions and thus the β and n_2 values. In order to determine the nonlinear optical contribution

TABLE I. A comparison table of the β and n_2 values of ZnO thin films and NRs using 532-nm excitation, from previous reports and the present study.

Sample	β(cm W^{-1})	n_2(cm^2 W^{-1})	Parameters	References
ZnO thin films	4.2×10^{-9}	-0.9×10^{-14}	$\lambda = 532$ nm, pulse width = 25 ps	[47]
ZnO thin films	4.68×10^{-3}	-1.37×10^{-8}	$\lambda = 532$ nm, cw laser	[48]
5%-Co–ZnO thin films	7.53×10^{-3}	-1.94×10^{-8}	$\lambda = 532$ nm, cw laser	[48]
ZnO nanoparticles (NPs)	2.55×10^{-7}	-7.79×10^{-13}	$\lambda = 532$ nm, cw laser	[49]
5%-Eu–ZnO NPs	-6.8×10^{-6}	4.67×10^{-13}	$\lambda = 532$ nm, cw laser	[49]
ZnO nanocolloids	2.37×10^{-7}	-1.55×10^{-12}	$\lambda = 532$ nm, pulse width = 7 ns	[50]
Ag-ZnO nanowire	-2.42×10^{-8}	4.4×10^{-13}	$\lambda = 532$ nm, pulse width = 4 ns	[51]
Graphene-ZnO NPs	-5.97×10^{-3}	1.183×10^{-9}	$\lambda = 532$ nm, cw laser	[52]
5%-Co–ZnO NPs	6.71×10^{-3}	6.02×10^{-8}	$\lambda = 532$ nm, cw laser	[53]
ZnO NRs	3.5×10^{-5}	-2.1×10^{-10}	$\lambda = 532$ nm, pulse width = 0.7 ns	[3]
2.5%-Mn–ZnO NRs	5.45×10^{-6}	-1.34×10^{-10}	$\lambda = 532$ *nm*, pulse width = 0.7 ns	[3]
ZnO NRs	9.16×10^{-5}	-6.35×10^{-10}	$\lambda = 532$ nm, pulse width = 1.1 ns	This work
1%-Co-doped ZnO NRs	-2.29×10^{-5}	-2.13×10^{-10}	$\lambda = 532$ nm, pulse width = 1.1 ns	This work
2%-Co-doped ZnO NRs	-2.36×10^{-5}	-4.65×10^{-10}	$\lambda = 532$ nm, pulse width = 1.1 ns	This work
3%-Co-doped ZnO NRs	-1.34×10^{-4}	-1.52×10^{-9}	$\lambda = 532$ nm, pulse width = 1.1 ns	This work
4%-Co-doped ZnO NRs	-2.26×10^{-4}	-1.56×10^{-9}	$\lambda = 532$ nm, pulse width = 1.1 ns	This work
5%-Co-doped ZnO NRs	-3.15×10^{-4}	-1.73×10^{-9}	$\lambda = 532$ nm, pulse width = 1.1 ns	This work

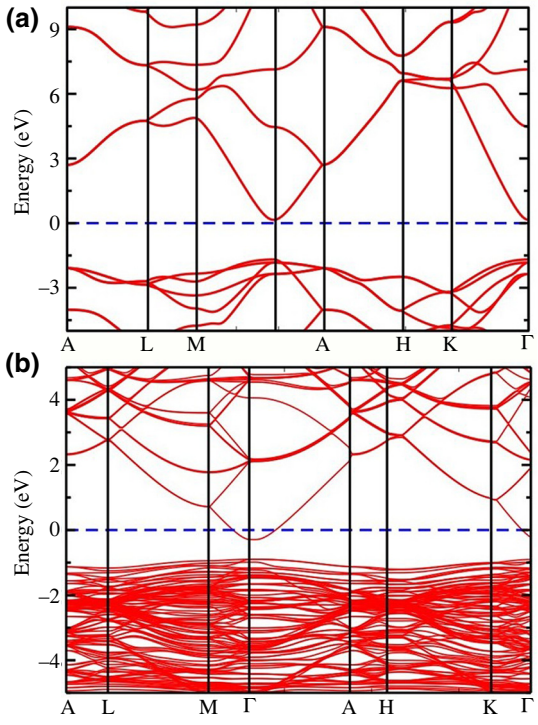

FIG. 10. The calculated electronic band structure of (a) pristine and (b) cobalt-doped ZnO. The dashed blue line at 0 eV denotes the Fermi level.

from the quartz substrate, the Z-scan measurements are also performed on the quartz substrate in the same conditions. The measurements reveal negligible variations in the normalized transmittance, which rules out the contribution from the substrate [3,26]. In the two-parabolic-band (TPB) theory and the Kramer-Kronig relation, it is said that ZnO, being a semiconductor, will show a negative nonlinear refractive index, since the excitation energy is above $0.7E_g$ and its sign changes at about two thirds of the band gap [6,7,46], which explains the observed negative n_2 values.

The calculated electronic band structures for the pristine and the cobalt-doped ZnO are shown in Fig. 10. The band gap of the pristine ZnO is calculated to be 1.84 eV. The valence-band maxima and the conduction-band minima occur at the same gamma point, so ZnO has a direct band gap. In the case of Co-doped ZnO, the conduction-band minima cross below the Fermi level and the band gap reduces to 0.60 eV. However, it is found that the calculated band gap of ZnO is lower than the experimental value. This is because of the well-known fact that, in general, DFT calculations using GGA tend to underestimate the band gap compared to the experimental value [54], whereas the reduction of the band gap is consistent in both calculation and experiment.

To understand the cause of the lowering of the band gap, we further calculate the partial density of states (PDOS). From Fig. 11, we see that in the case of pure ZnO, the valence band mainly consists of Zn-3d and O-2p states and the conduction band consists of Zn-4s and O-2p states. For Co-doped ZnO in Fig. 12, new localized density of states (DOS) peaks consisting of the Co-3d state appear very close to the Fermi level. This results in a decrease in the band gap as observed and the presence of such Co-related defect states near the Fermi level greatly enhances the probability that an electron will jump over to the conduction band from the valance band. Therefore, these defect states can facilitate SA by providing an intermediate state by means of which the valence electrons can reach the conduction band.

The variation of the nonlinear absorption coefficient (β) with the band gap of the ZnO nanorods is given in Fig. 13. With an increase in Co doping, we observe that the band gap does not change significantly but the β value changes and it follows an approximately logistic fit. To understand the observed SA in the Co-doped ZnO nanorods, we need to understand the defect-related electronic band modification arising due to the incorporation of Co^{2+} ions in the ZnO lattice. The nonlinear absorption is related to the energy band gap (E_g) of the material and the defect density in the crystal lattice. This means that the sign of β initially depends on the band gap of the material and that the SA characteristics increase with the increase of defect density. In case of the undoped NRs, since the excitation photon energy is more than half of the band-gap energy, an electron in the valence band can absorb two photons simultaneously and reach the conduction band [12]. But in the case of the doped NRs, it is known that the substitution of the Zn^{2+} by Co^{2+} gives rise to impurity-related narrow bands in the forbidden gap and that they split further due to the crystal field [55]. From our DFT calculations also, it is evident that the conduction-band minima come below the Fermi level and that new localized defect states are created near the Fermi level after incorporation of cobalt in the ZnO lattice. Now, with the increase in the amount of the doping concentration, the number of defect-related states per unit volume, i.e., the defect density in the crystal, also increases and more electrons are trapped in these defect states, which in turn also increases the lifetime of the electrons in the defect states [7]. Therefore, at high laser intensities, the defect states are filled very rapidly. In this way, the ground state is depopulated and thus the ground-state absorption is reduced [3]. Hence the combined effect of saturation of the defect states and depopulation of the ground state leads to the observed SA in the doped NRs.

Thus ZnO NRs can show both TPA and SA characteristics depending on the amount of Co doping and we can also tune the nonlinear absorption coefficient. The samples exhibiting TPA can be used in autocorrelators and optical power limiters [12]. Saturable absorbers are used in fiber lasers for passive Q switching [13] and passive mode locking [13], and these techniques are used for generating

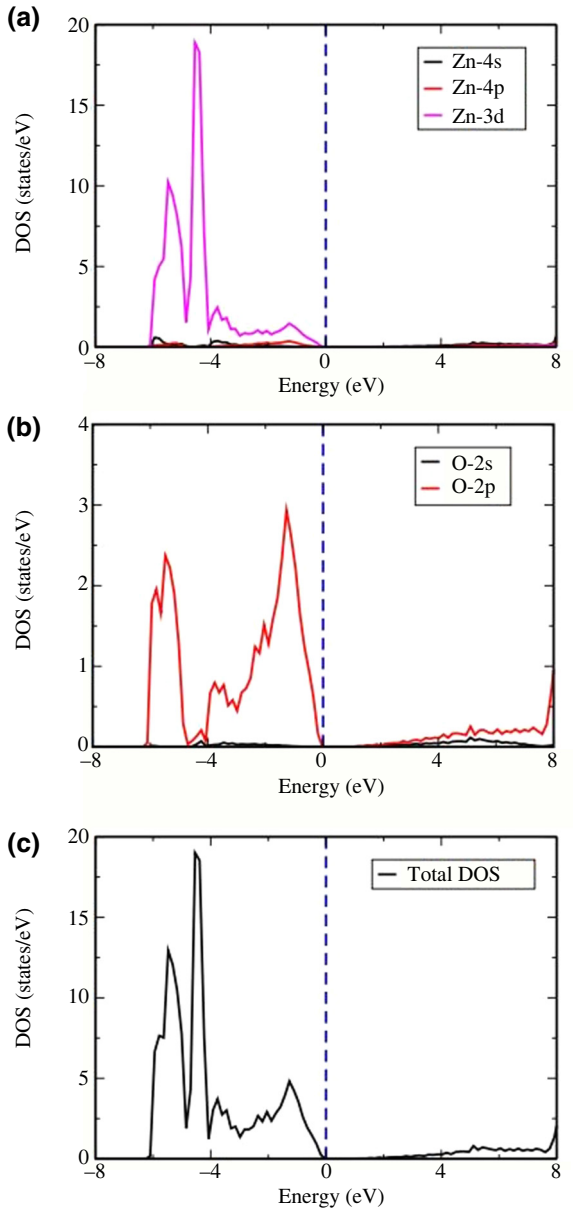

FIG. 11. The calculated PDOS of pristine ZnO with contributions (a) from Zn and (b) from O, and (c) the total DOS. The dashed blue line at 0 eV denotes the Fermi level.

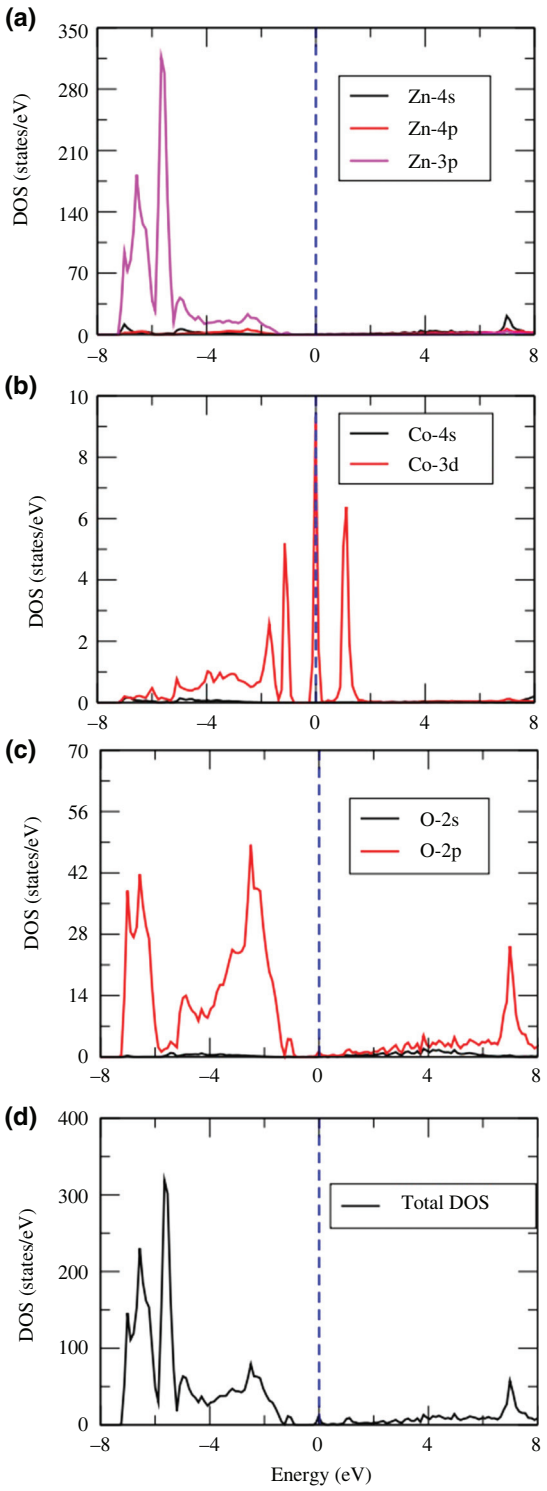

FIG. 12. The calculated PDOS of Co-doped ZnO with contributions (a) from Zn, (b) from Co, and (c) from O, and (d) the total DOS. The dashed blue line at 0 eV denotes the Fermi level.

highly energetic nanosecond and femtosecond laser pulses, respectively. TPA is a multiphoton absorption process. In the samples exhibiting TPA, when the laser irradiation is low, i.e., there are fewer photons, single-photon absorption (SPA) is the dominant phenomenon. However, this absorption is low, since the electrons cannot gain enough energy to reach the conduction band. This makes the undoped ZnO virtually transparent in the low-laser-power regime. When the laser irradiance is sufficiently high for the onset of TPA, the sample absorbs a significant number of photons, resulting in reduced transmission. Thus, we see that the transmission varies nonlinearly with the incident light intensity. Therefore, the undoped ZnO acts as an optical power limiter [56], i.e., it transmits low-intensity light and blocks high-intensity light. Nagaraja *et al.* [57] have shown that undoped ZnO thin films exhibiting TPA can

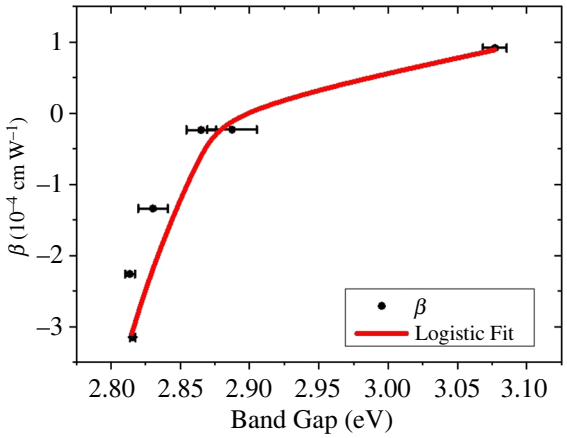

FIG. 13. Variation of the nonlinear absorption (β) with the band gap.

be effectively used as optical power limiters under the continuous-wave (cw) regime using a He-Ne laser ($\lambda =$ 633 nm). On the other hand, saturable absorbers favor transmission of high-intensity and absorb low-intensity light. When the doped ZnO is used in the laser resonator as a saturable absorber for passive Q switching [58], initially in the pumping phase, the light intensity in the resonator cavity is low and doped ZnO introduces losses. But as soon as the energy stored in the gain medium is sufficiently high, the laser pulse is generated. The light intensity then amplifies because of the energy stored in the gain medium through successive oscillations in the resonator. This leads to the saturation of the absorber, the losses introduced by it reduce, and the intensity increases even further. But as the time-integrated intracavity power reaches the saturation energy of the gain medium, the gain saturates, and the energy of the gain medium also depletes. This results in laser power decay and in the whole process, an output corresponding to a nanosecond laser pulse is generated. The next laser pulse remains due until the gain medium is sufficiently replenished [59]. Prieto-Cortés *et al.* [60] have successfully shown that 2% of Al-doped ZnO ($\beta = -4.8 \times 10^{-3}$ cm W^{-1}) can be used as a saturable absorber for passively Q switching a Er-Yb double-clad fiber laser. The SA property of doped ZnO can also find use in passive mode locking to generate femtosecond laser pulses, as shown by Ahmad *et al.* [61], using a $WS_2 - ZnO$ composite material. Here, a doped ZnO mirror can be placed at one end of the laser resonator. The doped ZnO mirror will absorb the weak pulses or continuous background light and allow the transmission and circulation of the high-intensity light. It also attenuates the leading and trailing wing of the circulating pulse, thus decreasing the pulse duration [62]. After many circulations, only the longitudinal modes of the laser resonator having a fixed phase relationship will survive and all the other modes of light pulses will be lost because of destructive interference in the resonator [59]. The modulation depth is a key parameter for passive mode locking and it is directly proportional to the nonlinear absorption coefficient [63]. Saturable absorbers with a large modulation depth have strong pulse-shaping properties and they can be useful to generate short laser pulses and design self-starting mode-locked lasers [64]. In a nutshell, Co-doped ZnO NRs with NLO properties can have a wide range of applications, depending on the properties that they exhibit.

IV. CONCLUSIONS

We grow undoped and cobalt-doped ZnO NRs hydrothermally and study the change in the morphological, structural, linear optical, and NLO properties of the NRs. We use a single-beam Z-scan technique to study the NLO properties of the NRs. The NLO properties of the NRs are linked to the linear optical absorption studies and we also understand the nonlinear absorption from the DFT calculations. The undoped NRs show TPA characteristics, whereas the doped NRs show SA characteristics in the OA measurements. Also, all the NRs show a self-defocusing effect in the CA measurements. The higher β and n_2 values can be attributed to the local enhancement of the field due to Fabry–Perot-like localized resonance, the defect states arising in the forbidden band gap, and the heating effect because of high irradiance of the laser. There is a change in the sign of the β value due to doping and its magnitude is found to increase with the doping concentration. The n_2 values are also found to increase at higher doping concentrations. Therefore, Co doping enhances the NLO interactions in the samples. ZnO NRs can have suitable applications as optical limiters or as saturable absorber materials in Q-switched and mode-locked solid-state and fiber lasers, depending on their properties and the amount of Co doping.

ACKNOWLEDGMENTS

We thank the National Institute of Science Education and Research, Department of Atomic Energy (DAE), India for the funding to carry out this work. We acknowledge Anupa Kumari and Ritwick Das for providing the facility for Z-scan measurements. M.K.S. would also like to acknowledge the University Grants Commission, India for financial support in the form of a University Grants Commission (UGC)—Council of Scientific and Industrial Research (CSIR) NET–Junior Research Fellowship (JRF)/Senior Research Fellowship (SRF) fellowship.

[1] K. Spoorthi, S. Pramodini, I. V. Kityk, M. Abd-Lefdil, M. Sekkati, A. E. Fakir, A. Rao, G. Sanjeev, and P. Poornesh, Investigations on nonlinear optical properties of electron beam treated Gd:ZnO thin films for photonic device applications, Laser Phys. **27**, 065403 (2017).

[2] A. Djurišić, A. Ng, and X. Chen, ZnO nanostructures for optoelectronics: Material properties and device applications, Prog. Quantum Electron. **34**, 191 (2010).

[3] A. Singh, S. Kumar, R. Das, and P. K. Sahoo, Defect-assisted saturable absorption characteristics in Mn doped ZnO nano-rods, RSC Adv. **5**, 88767 (2015).

[4] B. F. Levine, A New Contribution to the Nonlinear Optical Susceptibility Arising from Unequal Atomic Radii, Phys. Rev. Lett. **25**, 440 (1970).

[5] R. yao Wang, X. chun Wu, B. suo Zou, L. Wang, P. fei Wu, S. mei Liu, J. guo Wang, and J. ren Xu, Nonresonant optical nonlinearities of surface chemically modified ZnO composite nanoparticles, Chin. Phys. Lett. **15**, 27 (1998).

[6] L. Irimpan, A. Deepthy, B. Krishnan, L. Kukreja, V. Nampoori, and P. Radhakrishnan, Effect of self assembly on the nonlinear optical characteristics of ZnO thin films, Opt. Commun. **281**, 2938 (2008).

[7] K. M. Sandeep, S. Bhat, S. M. Dharmaprakash, P. S. Patil, and K. Byrappa, Defect assisted saturable absorption characteristics in Al and Li doped ZnO thin films, J. Appl. Phys. **120**, 123107 (2016).

[8] H. Fujiwara, T. Suzuki, R. Niyuki, and K. Sasaki, ZnO nanorod array random lasers fabricated by a laser-induced hydrothermal synthesis, New J. Phys. **18**, 103046 (2016).

[9] J. C. Johnson, K. P. Knutsen, H. Yan, M. Law, Y. Zhang, P. Yang, and R. J. Saykally, Ultrafast carrier dynamics in single ZnO nanowire and nanoribbon lasers, Nano Lett. **4**, 197 (2004).

[10] P. D. Dragic, M. Cavillon, and J. Ballato, Materials for optical fiber lasers: A review, Appl. Phys. Rev. **5**, 041301 (2018).

[11] M. N. Zervas and C. A. Codemard, High power fiber lasers: A review, IEEE J. Sel. Top. Quantum Electron. **20**, 219 (2014).

[12] R. Paschotta, in *Encyclopedia of Laser Physics and Technology* (Wiley-VCH, Berlin, 2008), 766, Vol. 1. ISBN 978-3-527-40828-3.

[13] R. Paschotta, *Encyclopedia of Laser Physics and Technology* (Wiley-VCH, Berlin, 2008), 650, Vol. 1. ISBN 978-3-527-40828-3.

[14] Z. L. Wang, Zinc oxide nanostructures: Growth, properties and applications, J. Phys.: Condens. Matter **16**, R829 (2004).

[15] L. Schmidt-Mende and J. L. MacManus-Driscoll, ZnO—Nanostructures, defects, and devices, Mater. Today **10**, 40 (2007).

[16] C.-F. Lo, B. S. Kang, S. J. Pearton, I. I. Kravchenko, and F. Ren, in *Semiconductor-Based Sensors*, (World Scientific, Singapore, 2016), Chap. 9, p. 299.

[17] J. Bao, M. A. Zimmler, F. Capasso, X. Wang, and Z. F. Ren, Broadband ZnO single-nanowire light-emitting diode, Nano Lett. **6**, 1719 (2006).

[18] K. Keis, E. Magnusson, H. Lindström, S.-E. Lindquist, and A. Hagfeldt, A 5% efficient photoelectrochemical solar cell based on nanostructured ZnO electrodes, Solar Energy Mater. Solar Cells **73**, 51 (2002).

[19] A. Pang, C. Chen, L. Chen, W. Liu, and M. Wei, Flexible dye-sensitized ZnO quantum dots solar cells, RSC Adv. **2**, 9565 (2012).

[20] V. Kumari, V. Kumar, D. Mohan, Purnima, B. Malik, R. Mehra, Effect of surface roughness on laser induced nonlinear optical properties of annealed ZnO thin films, J. Mater. Sci. Technol. **28**, 506 (2012).

[21] C.-L. Hsu and S.-J. Chang, Doped ZnO 1D nanostructures: Synthesis, properties, and photodetector application, Small **10**, 4562 (2014).

[22] A. Afaah, Z. Khusaimi, and M. Rusop, in *Nanosynthesis and Nanodevice*, Advanced Materials Research (Trans Tech Publications Ltd., Kreuzstrasse 10, CH-8635 Durnten-Zurich, 2013), Vol. 667. p. 329.

[23] T. Dietl, H. Ohno, F. Matsukura, J. Cibert, and D. Ferrand, Zener model description of ferromagnetism in zinc-blende magnetic semiconductors, Science **287**, 1019 (2000).

[24] D. P. Joseph and C. Venkateswaran, Bandgap engineering in ZnO by doping with 3D transition metal ions, J. At., Mol., Opt. Phys. **2011**, 7 (2011).

[25] M. Khalid, S. Riaz, and S. Naseem, Tailoring of the band gap in transition metal-doped ZnO: First principle calculations, Mater. Today: Proc. **2**, 5246 (2015). International Conference on Solid State Physics 2013 (ICSSP'13).

[26] T.-F. Yan, Y. Li, J.-J. Kang, P.-Y. Zhou, B.-Q. Sun, K. Zhang, S.-S. Yan, and X.-H. Zhang, The third-order nonlinear optical properties in cobalt-doped ZnO films, Chin. Phys. Lett. **32**, 077801 (2015).

[27] G. Kresse and J. Hafner, *Ab initio* molecular dynamics for liquid metals, Phys. Rev. B **47**, 558 (1993).

[28] G. Kresse and J. Furthmüller, Efficient iterative schemes for *ab initio* total-energy calculations using a plane-wave basis set, Phys. Rev. B **54**, 11169 (1996).

[29] J. P. Perdew, J. A. Chevary, S. H. Vosko, K. A. Jackson, M. R. Pederson, D. J. Singh, and C. Fiolhais, Atoms, molecules, solids, and surfaces: Applications of the generalized gradient approximation for exchange and correlation, Phys. Rev. B **46**, 6671 (1992).

[30] A. Kaphle and P. Hari, Variation of index of refraction in cobalt doped ZnO nanostructures, J. Appl. Phys. **122**, 165304 (2017).

[31] Y. Tong, Y. Liu, L. Dong, D. Zhao, J. Zhang, Y. Lu, D. Shen, and X. Fan, Growth of ZnO nanostructures with different morphologies by using hydrothermal technique, J. Phys. Chem. B **110**, 20263 (2006).

[32] M. Sheik-Bahae, A. A. Said, T. Wei, D. J. Hagan, and E. W. Van Stryland, Sensitive measurement of optical nonlinearities using a single beam, IEEE J. Quantum. Electron. **26**, 760 (1990).

[33] See the Supplemental Material at http://link.aps.org/supplemental/10.1103/PhysRevApplied.14.014050 for details of the TEM-EDS, XRD, and Raman analysis.

[34] T. M. Hammad, J. K. Salem, and R. G. Harrison, Structure, optical properties and synthesis of Co-doped ZnO superstructures, Appl. Nanosci. **3**, 133 (2013).

[35] F. A. Taher and E. Abdeltwab, Shape-controlled synthesis of nanostructured Co-doped ZnO thin films and their magnetic properties, CrystEngComm **20**, 5844 (2018).

[36] B. Cullity and S. Stock, *Elements of X-Ray Diffraction* (Prentice-Hall, New York, 2001), 3rd ed.

[37] V. Gupta and A. Mansingh, Influence of postdeposition annealing on the structural and optical properties of sputtered zinc oxide film, J. Appl. Phys. **80**, 1063 (1996).

[38] S. Maniv, W. D. Westwood, and E. Colombini, Pressure and angle of incidence effects in reactive planar magnetron sputtered ZnO layers, J. Vac. Sci. Technol. **20**, 162 (1982).

[39] W. Baiqi, S. Xudong, F. Qiang, J. Iqbal, L. Yan, F. Honggang, and Y. Dapeng, Photoluminescence properties of Co-doped ZnO nanorods array fabricated by the solution method, Phys. E: Low-Dimensional Syst. Nanostruct. **41**, 413 (2009).

[40] M. Sajjad, I. Ullah, M. Khan, J. Khan, M. Y. Khan, and M. T. Qureshi, Structural and optical properties of pure and copper doped zinc oxide nanoparticles, Results Phys. **9**, 1301 (2018).

[41] Y. Lü, Q. Zhou, L. Chen, W. Zhan, Z. Xie, Q. Kuang, and L. Zheng, Templated synthesis of diluted magnetic semiconductors using transition metal ion-doped metal–organic frameworks: The case of Co-doped ZnO, CrystEngComm **18**, 4121 (2016).

[42] J. Menéndez and M. Cardona, Temperature dependence of the first-order Raman scattering by phonons in Si, Ge, and $\alpha - \mathrm{Sn}$: Anharmonic effects, Phys. Rev. B **29**, 2051 (1984).

[43] T. Gruber, G. M. Prinz, C. Kirchner, R. Kling, F. Reuss, W. Limmer, and A. Waag, Influences of biaxial strains on the vibrational and exciton energies in ZnO, J. Appl. Phys. **96**, 289 (2004).

[44] S. B. Yahia, L. Znaidi, A. Kanaev, and J. Petitet, Raman study of oriented ZnO thin films deposited by sol-gel method, Spectrochim. Acta Part A: Mol. Biomol. Spectrosc. **71**, 1234 (2008).

[45] P. M. Kibasomba, S. Dhlamini, M. Maaza, C.-P. Liu, M. M. Rashad, D. A. Rayan, and B. W. Mwakikunga, Strain and grain size of TiO_2 nanoparticles from TEM, Raman spectroscopy and XRD: The revisiting of the Williamson-Hall plot method, Results Phys. **9**, 628 (2018).

[46] K. Nagaraja, S. Pramodini, A. S. Kumar, H. Nagaraja, P. Poornesh, and D. Kekuda, Third-order nonlinear optical properties of Mn doped ZnO thin films under cw laser illumination, Opt. Mater. **35**, 431 (2013).

[47] X. Zhang, H. Fang, S. Tang, and W. Ji, Determination of two-photon-generated free-carrier lifetime in semiconductors by a single-beam *Z*-scan technique, Appl. Phys. B **65**, 549 (1997).

[48] R. Bairy, P. s. Patil, S. R. Maidur, H. Vijeth, M. S. Murari, and K. Udaya Bhat, The role of cobalt doping in tuning the band gap, surface morphology and third-order optical nonlinearities of ZnO nanostructures for NLO device applications, RSC Adv. **9**, 22302 (2019).

[49] U. Vinoditha, B. K. Sarojini, K. M. Sandeep, B. Narayana, S. R. Maidur, P. S. Patil, and K. M. Balakrishna, Defects-induced nonlinear saturable absorption mechanism in europium-doped ZnO nanoparticles synthesized by facile hydrothermal method, Appl. Phys. A **125**, 436 (2019).

[50] M. Ramya, T. Nideep, K. Vijesh, V. Nampoori, and M. Kailasnath, Synthesis of stable ZnO nanocolloids with enhanced optical limiting properties via simple solution method, Opt. Mater. **81**, 30 (2018).

[51] K.-X. Zhang, C.-B. Yao, X. Wen, Q.-H. Li, and W.-J. Sun, Ultrafast nonlinear optical properties and carrier dynamics of silver nanoparticle-decorated ZnO nanowires, RSC Adv. **8**, 26133 (2018).

[52] E. Solati and D. Dorranian, Nonlinear optical properties of the mixture of ZnO nanoparticles and graphene nanosheets, Appl. Phys. B **122**, 76 (2016).

[53] R. Ponnusamy, D. Sivasubramanian, P. Sreekanth, V. Gandhiraj, R. Philip, and G. M. Bhalerao, Nonlinear optical interactions of Co: ZnO nanoparticles in continuous and pulsed mode of operations, RSC Adv. **5**, 80756 (2015).

[54] P. Erhart, K. Albe, and A. Klein, First-principles study of intrinsic point defects in ZnO: Role of band structure, volume relaxation, and finite-size effects, Phys. Rev. B **73**, 205203 (2006).

[55] H. Yang and S. Nie, Preparation and characterization of Co-doped ZnO nanomaterials, Mater. Chem. Phys. **114**, 279 (2009).

[56] F. J. Aranda, M. T. Harris, M. J. Callahan, J. S. Bailey, M. J. Suscavange, D. F. Bliss, B. R. Kimball, M. Nakashima, B. S. DeCristofano, and D. V. G. L. N. Rao, in *Power-Limiting Materials and Devices*, edited by C. M. Lawson, International Society for Optics and Photonics (SPIE, Denver, Colorado, 1999), Vol. 3798, p. 22.

[57] K. K. Nagaraja, S. Pramodini, P. Poornesh, and H. S. Nagaraja, Effect of annealing on the structural and nonlinear optical properties of ZnO thin films under cw regime, J. Phys. D: Appl. Phys. **46**, 055106 (2013).

[58] R. Paschotta, in *Encyclopedia of Laser Physics and Technology* (Wiley-VCH, Berlin, 2008), 588, Vol. 1. ISBN 978-3-527-40828-3.

[59] B. Denker and E. Shklovsky, eds., *Handbook of Solid-State Lasers*, Woodhead Publishing Series in Electronic and Optical Materials (Woodhead Publishing, 2013).

[60] P. Prieto-Cortés, R. I. Álvarez-Tamayo, M. García-Méndez, M. Durán-Sánchez, A. Barcelata-Pinzón, and B. Ibarra-Escamilla, Magnetron sputtered Al-doped ZnO thin film as saturable absorber for passively *Q*-switched Er/Yb double clad fiber laser, Laser Phys. Lett. **16**, 045101 (2019).

[61] H. Ahmad, H. Monajemi, M. Z. Samion, N. Yusoff, M. F. Ismail, M. Yasin, and L. Bayang, Near-infrared soliton mode-locked thulium doped fibre laser using WS_2-ZnO composite material as saturable absorber, IEEE Photonics J. **11**, 1 (2019).

[62] R. Paschotta, in *Encyclopedia of Laser Physics and Technology* (Wiley-VCH, Berlin, 2008), 507, Vol. 1. ISBN 978-3-527-40828-3.

[63] L. C. Gómez-Pavón, G. J. Lozano-Perera, A. Luis-Ramos, J. M. M. noz Pacheco, J. P. Padilla-Martínez, and P. Zaca-Morán, Influence on the saturable absorption of the induced losses by photodeposition of zinc nanoparticles in an optical fiber, Opt. Express **26**, 1556 (2018).

[64] L. Cheng, Y. Yuan, C. Liu, X. Cao, J. Su, X. Zhang, H. Zhang, H. Zhao, M. Xu, and J. Li, Linear and nonlinear optical properties modulation of Sb_2Te_3/GeTe bilayer film as a promising saturable absorber, Results Phys. **13**, 102282 (2019).